Improved Energy Balancing of Grid-Side Modular Multilevel Converters by Optimized Feedforward Circulating Currents and Common-Mode Voltage

Hendrik Fehr and Albrecht Gensior

***Abstract*—In contrast to the conventional feedback approach, the energy balancing task of a grid-side modular multilevel converter (MMC) with half-bridge cells and an isolated ac star point is considered as an optimization problem. As a result, nominal trajectories for circulating currents and common-mode voltage are obtained that inherently steer the system back to a balanced operation within finite time. The method relies on an MMC arm energy model, allowing for algebraic parameterization of almost all MMC variables during optimization, which considerably reduces the computational cost. Thus, the optimized solution is the one selected from a family of trajectories that meets the balancing goal. Owing to the trajectory planning of the MMC energies, the search for a solution is inherently limited to the domain of realistic energy variations and no balancing error remains even during transfers between operating regimes, i.e., the task of the balancing controller is reduced to the compensation of parameter uncertainties and disturbances. Here, a grid-side MMC is considered in the optimization in contrast to the previous work, which has been restricted to passive RL loads. Measurement results reveal drawbacks of the previous solution after adoption of a grid-side application. A dedicated candidate transfer for grid-side applications eliminate the drawbacks and regains the improved balancing performance as shown by measurements.**

***Index Terms*—Control systems, modeling, modular multilevel converter (MMC), tracking control.**

I. Introduction

THE topology of modular multilevel converters (MMCs) consists of two arms per phase each equipped with a series connection of half-bridge or full-bridge cells and arm inductors to suppress circulating currents [1]. This enables fault-tolerant generation of multilevel voltages and favors the use in medium- and high-voltage applications [2]–[5]. Cell capacitor voltage control in MMCs is challenging, because the one-port nature of the arms demands a balanced energy exchange over time. This complicates the adherence to a desired cell-voltage band.

The aim of MMC energy balancing is to reach the same average cell voltage for all arms in a stationary operation, after a change of the operating regime, during fault-ride-through conditions [6], [7], and in the presence of (unbalanced) integration of energy storage devices [8], [9], or when feeding pulsed dc loads [10]. This balancing task is challenging because an impact on the ac currents must be avoided. In the most demanding case, it is even not allowed to change the dc current. Hence, the common-mode voltage and the circulating currents are used to generate additional power components in the arms dedicated to balancing, e.g., [11]–[19]. This enables stable and balanced operation during stationary regimes. However, after load steps, the system leaves the stationary operating regime and it usually takes some time to restore a balanced operation due to the mutual interactions. Although mathematical optimization has been applied to the MMC control problem [15], [20], feedback-balancing schemes dominate the current literature. So far, feedforward signals have been obtained assuming stationary regimes, e.g., for 0 Hz operation [16], [18], capacitor voltage ripple reduction [21], [22], or periodic loads [10]. This research deficit originates from the difficulty of calculating feedforward circulating currents and common-mode voltage while simultaneously satisfying the multiple conflicting balancing requirements.

This motivates the method presented here that can roughly be summarized as follows: For a given transient, trajectories of the circulating currents and the common-mode voltage can be calculated in advance that force the system back to a balanced operation within finite time. In the implementation of the method, these trajectories are injected by a feedforward. As a benefit, balancing already takes place during the transient maneuver and not as a response to an already existing imbalance as it is the case for a pure feedback-based scheme. Thus, the balanced operation can be restored faster and the imbalance can be kept smaller. An early version of this idea has been applied to a single-phase system in [23]. Unfortunately, the algebraic solution found there is not applicable to the three-phase system. Furthermore, one of the energies was steered in open loop only. These problems have been addressed by the conference paper [24] and this paper extends these preliminary results as follows.

1) In [24], an RL load has been used for a quick validation of the method in a simplified setup. In order to further investigate the method, here a more industry-relevant application is used by connecting the MMC to the grid. This comes along with several difficulties, e.g., the reserve for the common-mode voltage is much smaller.

Manuscript received November 28, 2017; revised January 22, 2018; accepted January 29, 2018. Date of publication February 12, 2018; date of current version September 28, 2018. This work was supported by the Deutsche Forschungsgemeinschaft under Grant GE 2502/4-1. Recommended for publication by Associate Editor M. Hagiwara. *(Corresponding author: Hendrik Fehr.)*

The authors are with the Professur Leistungselektronik, Elektrotechnisches Institut, Technische Universität Dresden, Dresden 01069, Germany (e-mail: hendrik.fehr@mailbox.tu-dresden.de; albrecht.gensior@tu-dresden.de).

Color versions of one or more of the figures in this paper are available online at http://ieeexplore.ieee.org.

Digital Object Identifier 10.1109/TPEL.2018.2805103

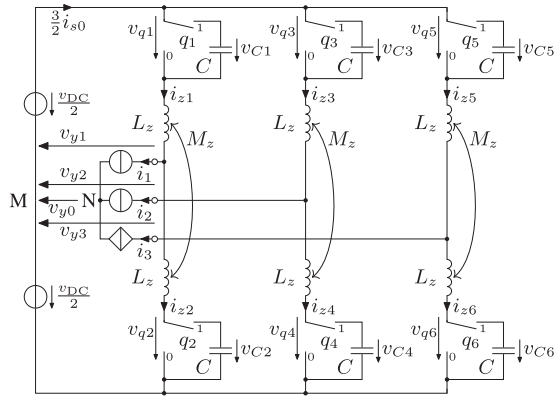

Fig. 1. Continuous model of an MMC using equivalent cells. The cells of each arm are represented by equivalent cells and their duty cycles $q_k \in [0,1]$, $k = 1,\ldots,6$, are used as control inputs. The load is given by current sources i_1, i_2, and the controlled current source $i_3 = -i_1 - i_2$ to ensure compliance with Kirchoff's first law at *N*. The load currents are assumed to be continuous and to match to the initial currents of the inductors.

2) In view of the new application, the method has been extended for an improved common-mode voltage.
3) Comparing to the conference paper [24], the text has been improved for a better insight, in particular, regarding the modeling and the method itself. Furthermore, more experimental results are provided.

Thus, this paper presents a trajectory-planning-based solution to symmetrize the energies of a three-phase MMC. After setpoint transitions, a symmetrical operation is restored in finite time, which is demonstrated experimentally by feeding a passive load and grid. For the latter, the control algorithm used for the former is enhanced, which shows that the method allows to incorporate further technical requirements by a suitable choice of trajectories. Thus, the present contribution is a proof of concept for the trajectory-planning-based control of MMCs showing potential improvements over existing control methods but also discussing the limits where further research is required.

This paper is organized as follows: A model of the MMC arm energies and the parameterization of its variables are given in Section II in order to prepare for the explanation of the optimization in Section III where, the integration of standard balancing into the optimized scheme is explained as well. Section IV reports measurement results for an RL load and for a grid-side setup in order to compare the balancing methods. Conclusions are given in Section V.

II. Modeling

A. MMC Model

For modeling the MMC in Fig. 1, the following assumptions are made.

1) The cells of arm $k = 1,2,\ldots,6$ are represented by one equivalent cell [3], [25] with the duty cycle $q_k \in [0,1]$ and a voltage v_{Ck} that accords the sum of the voltages of the individual cells in the arm. This implies that the underlying problem of balancing the voltages within each arm has already been solved.
2) The load currents are assumed to be continuous, matched to the initial currents of the arm inductors, and satisfy the constraint $i_1 + i_2 + i_3 = 0$ caused by junction *N*.

Instead of using the voltages v_{Ck} to describe the behavior of the system, the arm energy variables e_{zk}, $k = 1,\ldots,6$, are used. For example, the upper and lower arm energies of the first phase are given by

$$e_{z1} = \frac{1}{2}Cv_{C1}^2 + \frac{1}{2}(L_z + M_z)i_{z1}^2 - \frac{1}{4}M_z i_1^2 \tag{1a}$$

$$e_{z2} = \frac{1}{2}Cv_{C2}^2 + \frac{1}{2}(L_z + M_z)i_{z2}^2 - \frac{1}{4}M_z i_1^2 \tag{1b}$$

in which v_{C1} and v_{C2} are the equivalent cell voltages and i_{z1}, i_{z2}, and i_1 denote the arm currents of the respective arm and the output current of the first phase. The six arm energies $e_{z1},\ldots,e_{z6}$ are transformed as

$$e_{s0} = 2g_0\left[(e_{z1},e_{z3},e_{z5})^T + (e_{z2},e_{z4},e_{z6})^T\right] \tag{2a}$$

$$e_{d0} = 2g_0\left[(e_{z1},e_{z3},e_{z5})^T - (e_{z2},e_{z4},e_{z6})^T\right] \tag{2b}$$

$$\underline{e}_s = 2\underline{g}_{\alpha\beta}\left[(e_{z1},e_{z3},e_{z5})^T + (e_{z2},e_{z4},e_{z6})^T\right] \tag{2c}$$

$$\underline{e}_d = 2\underline{g}_{\alpha\beta}\left[(e_{z1},e_{z3},e_{z5})^T - (e_{z2},e_{z4},e_{z6})^T\right] \tag{2d}$$

using the Clarke Transform

$$T_{0\alpha\beta} = \frac{1}{3}\begin{pmatrix}1 & 1 & 1\\ 2 & -1 & -1\\ 0 & \sqrt{3} & -\sqrt{3}\end{pmatrix} = \begin{pmatrix}g_0\\ g_\alpha\\ g_\beta\end{pmatrix} \tag{3}$$

and $\underline{g}_{\alpha\beta} = e^{-j\theta}\,(g_\alpha + jg_\beta)$. The variable e_{s0} denotes the total stored energy (scaled by $2/3$) and e_{d0} denotes the (vertical) difference between all upper and all lower arms (scaled by $2/3$ as well). The complex energy sum $\underline{e}_s$ and energy difference $\underline{e}_d$ are given in a rotating reference frame with angle θ. Together with the vertical difference e_{d0}, they represent the alternating part of the arm energies in the stationary operation.

The currents can be transformed similarly as

$$i_{s0} = g_0\left[(i_{z1},i_{z3},i_{z5})^T + (i_{z2},i_{z4},i_{z6})^T\right] \tag{4a}$$

$$0 = g_0(i_1,i_2,i_3)^T \tag{4b}$$

$$\underline{i}_s = \underline{g}_{\alpha\beta}\left[(i_{z1},i_{z3},i_{z5})^T + (i_{z2},i_{z4},i_{z6})^T\right] \tag{4c}$$

$$\underline{i} = \underline{g}_{\alpha\beta}(i_1,i_2,i_3)^T \tag{4d}$$

where i_{s0} is a scaled version of the dc current, $\underline{i}_s$ denotes the circulating current, and $\underline{i}$ is the output current in complex notation. The sum of the load currents is zero as can be seen from (4b).

Equivalently, the voltages are transformed as

$$v_{x0} = g_0\big[v_{\mathrm{DC}}(1,1,1)^T - (v_{q1}, v_{q3}, v_{q5})^T - (v_{q2}, v_{q4}, v_{q6})^T\big] \tag{5a}$$

$$v_{y0} = g_0(v_{y1}, v_{y2}, v_{y3})^T \tag{5b}$$

$$\underline{v}_x = \underline{g}_{\alpha\beta}\big[v_{\mathrm{DC}}(1,1,1)^T - (v_{q1}, v_{q3}, v_{q5})^T - (v_{q2}, v_{q4}, v_{q6})^T\big] \tag{5c}$$

$$\underline{v}_y = \underline{g}_{\alpha\beta}(v_{y1}, v_{y2}, v_{y3})^T \tag{5d}$$

$$= \underline{g}_{\alpha\beta}\Big[(v_{q2}, v_{q4}, v_{q6})^T - (v_{q1}, v_{q3}, v_{q5})^T - (L_z - M_z)\tfrac{\mathrm{d}}{\mathrm{d}t}(i_1, i_2, i_3)^T\Big] \tag{5e}$$

where v_{y0} denotes the common-mode voltage and $\underline{v}_y$ the complex output voltage. The voltages v_{x0} and $\underline{v}_x$ drive the dc current and internal currents, respectively.

In these coordinates, the model of the MMC arm energies reads

$$\dot{e}_{s0} = v_{\mathrm{DC}} i_{s0} - \mathrm{Re}\big(\underline{i}\,\underline{v}_y^*\big) \tag{6a}$$

$$\dot{e}_{d0} = -2v_{y0} i_{s0} - \mathrm{Re}\big(\underline{i}_s^*\underline{v}_{y\Delta}\big) \tag{6b}$$

$$\underline{\dot{e}}_s = v_{\mathrm{DC}}\underline{i}_s - \mathrm{e}^{-j3\theta}\underline{v}_y^*\underline{i}^* - 2\underline{i}\,v_{y0} - j\omega\underline{e}_s \tag{6c}$$

$$\underline{\dot{e}}_d = v_{\mathrm{DC}}\underline{i} - \mathrm{e}^{-j3\theta}\underline{i}_s^*\underline{v}_{y\Delta}^* - 2\underline{i}_s v_{y0} - 2i_{s0}\underline{v}_{y\Delta} - j\omega\underline{e}_d \tag{6d}$$

with the angular speed $\omega = \frac{\mathrm{d}}{\mathrm{d}t}\theta$ of the reference frame and the voltage

$$\underline{v}_{y\Delta} = \underline{v}_y - M_z\left(j\omega\underline{i} + \tfrac{\mathrm{d}}{\mathrm{d}t}\underline{i}\right). \tag{7}$$

In case there is no magnetic coupling between the inductors, $M_z = 0$ and therefore $\underline{v}_{y\Delta} = \underline{v}_y$. In order to get the idea, the reader may assume this case first which in the following leads to some simplifications. The model is completed by the dynamics of the circulating current $\underline{i}_s$ and the (scaled) dc current i_{s0}

$$(L_z + M_z)\frac{\mathrm{d}}{\mathrm{d}t}\underline{i}_s = \underline{v}_x - j\omega(L_z + M_z)\underline{i}_s \tag{8a}$$

$$(L_z + M_z)\frac{\mathrm{d}}{\mathrm{d}t}i_{s0} = v_{x0} \tag{8b}$$

while the output current $\underline{i}$ and its derivative $\frac{\mathrm{d}}{\mathrm{d}t}\underline{i}$ assume the role of time-dependent parameters.

Summing up, during the modeling process, no further simplifying assumptions have been made and the model in the transformed variables still describes the behavior of the circuit shown in Fig. 1, i.e., apart from transformations, the MMC model (6), (8) is equivalent to a representation found by applying Kirchhoff's circuit laws. Using the inverse of the transformations applied above, the quantities i_{zk}, v_{Ck}, q_k, $k = 1, 2, \ldots, 6$, and i_1, i_2, i_3 can be retrieved.

Although, at a first glance, our choice of variables may appear more complicated, it offers the following advantages.

1) Separation of the load: The variables of the load assume the role of time-dependent parameters of the MMC model. This allows to separate the tasks of controlling the load from the balancing problem, see Section II-B for further details.
2) Readily accessible stationary solutions: Stationary solutions of the energy subsystem (6) can easily be obtained as discussed in Section II-C.
3) Parameterization via e_{s0}, $\underline{e}_s$, and e_{d0}: The energies e_{s0}, $\underline{e}_s$, and e_{d0} and their derivatives $\dot{e}_{s0}$, $\ddot{e}_{s0}$, $\underline{\dot{e}}_s$, $\underline{\ddot{e}}_s$, and $\dot{e}_{d0}$ can be used to calculate the circulating current $\underline{i}_s$ and its driving voltage $\underline{v}_x$, the dc current i_{s0}, and its driving voltage v_{x0} as well as the common-mode voltage v_{y0}. This is demonstrated in Section II-D.

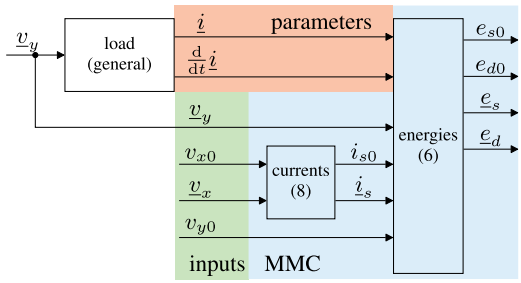

Fig. 2. MMC model consisting of the energy and current subsystem (6) and (8), respectively. The variables of the load assume the role of time-dependent parameters in the context of the MMC model [24].

B. Separation of the Load

In practice, the control of the load fixes the voltage $\underline{v}_y$. Although the MMC has to provide this voltage to the load, it remains unavailable for the balancing control of the MMC. This motivates to discuss both tasks separately. From the perspective of controlling the MMC and consequently in the modeling above, the load is considered as a current source. This led $\underline{i}$ and $\frac{\mathrm{d}}{\mathrm{d}t}\underline{i}$ play the role of parameters in the MMC energy subsystem (6), which is illustrated by the block diagram in Fig. 2.

Now, it remains to specify these parameters. In our approach, this is done by solving the control problem for the load first and tackling the balancing task second. For this purpose, a load model is required. For the applications considered here, the following is used:

$$L\frac{\mathrm{d}}{\mathrm{d}t}\underline{i} = \underline{v}_y - (R + j\omega L)\underline{i} - \underline{v}_g \tag{9}$$

with R and L being the resistance and inductance of the load. The voltage $\underline{v}_g$ enables the model to be used for grid applications by modeling the grid voltage.

The reference trajectory $t \mapsto \underline{i}_{\mathrm{d}(t)}$ for the output current $\underline{i}$ is a linear transfer between $\underline{I}_A$ and $\underline{I}_B$, given by

$$\underline{i}_{\mathrm{d}} = \underline{I}_A + (\underline{I}_B - \underline{I}_A)F_1(\tau_{\mathrm{L}}), \quad \tau_{\mathrm{L}} = \frac{t}{T_{\mathrm{L}}} \tag{10}$$

in which F_1 is defined in Table I and depicted in Fig. 3(a).

The controller

$$\underline{v}_y = \underline{v}_g + (R + j\omega L)\underline{i} + K_p\left(\underline{i}_{\mathrm{d}} - \underline{i}\right) + L\frac{\mathrm{d}}{\mathrm{d}t}\underline{i}_{\mathrm{d}} \tag{11}$$

TABLE I
DEFINITION OF FUNCTIONS F_1, F_2, AND F_3

	$\tau < 0$	$0 \leq \tau \leq 1$	$\tau > 1$
$F_1(\tau)$	0	τ	1
$F_2(\tau)$	0	$\sin^2(\tau\frac{\pi}{2})$	1
$F_3(\tau)$	0	$\sin(\tau\frac{\pi}{2}) - F_2(\tau)$	0

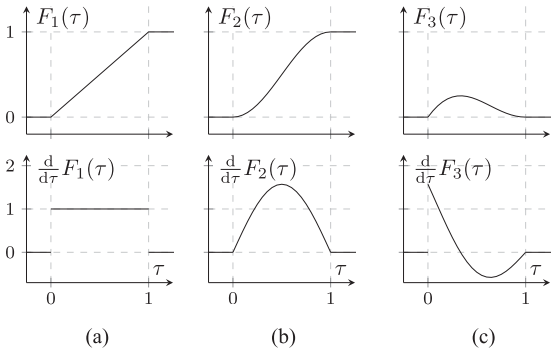

Fig. 3. In order to ease trajectory planning, the functions F_1, F_2, and F_3, defined in Table I, are used [24]. (a) Linear ramp. (b) Smooth ramp. (c) Controlled ramp.

with positive gain K_p ensures asymptotic stability of the load current $\underline{i}$ w.r.t. its desired trajectory $\underline{i}_d$.

Taking again the perspective for controlling the MMC, the parameters describing the load can now be specified as follows.

1) For trajectory planning, the nominal behavior of the load is defined by $\underline{i}_\mathrm{d}$ and $\frac{\mathrm{d}}{\mathrm{dt}}\underline{i}_\mathrm{d}$. The nominal version of the output voltage $\underline{v}_y$ can be obtained from (9) once the current trajectory (10) and its derivative have been inserted.
2) For the control design of the MMC, the actual values are required instead of the nominal ones. The load current $\underline{i}$ is provided by measurement, whereas $\frac{\mathrm{d}}{\mathrm{d}t}\underline{i}$ is obtained from the model (9), after controller (11) has been inserted. The voltage $\underline{v}_y$ to be realized by the MMC is given by (11).

Thus, in either case, the quantities describing the load are known. As a benefit, this technique of hiding the control of the output currents from the balancing problem ensures that the trajectories of the load are by principle not affected by the balancing scheme.

C. Stationary Operating Regime

Energy balancing in stationary operating regimes benefits from a good prediction of the arm energies' alternating components. Here, the prediction is based on a solution of the energy model (13), which will be extended to the nonstationary operation in Section III-A. Assuming, for example, a constant output current $\underline{i} = \underline{I}$ and voltage $\underline{v}_y = \underline{V}_y$, and a triplen harmonic injection of the common-mode voltage as

$$v_{y0} = -\frac{|\underline{V}_y|}{6}\mathrm{Re}\Big(\mathrm{e}^{j3(\theta+\arg\underline{V}_y)}\Big) \tag{12}$$

while demanding zero circulating current, i.e., $\underline{i}_s \equiv 0$, the solution of (6) can be written as

$$e_{s0} = E_{s0} \tag{13a}$$
$$e_{d0} = \mathrm{Re}\big(\underline{E}_{d0}\mathrm{e}^{j3\theta}\big) \tag{13b}$$
$$\underline{e}_s = \underline{E}_{s,p}\mathrm{e}^{j3\theta} + \underline{E}_{s,n}\mathrm{e}^{-j3\theta} \tag{13c}$$
$$\underline{e}_d = \underline{E}_d \tag{13d}$$

by using the constants E_{s0}, and

$$\underline{E}_{d0} = -j\frac{I_{s0}\,|\underline{V}_y|}{9\omega}\mathrm{e}^{j3\arg\underline{V}_y} \tag{14a}$$
$$\underline{E}_{s,p} = -j\frac{\underline{I}\,|\underline{V}_y|}{24\omega}\mathrm{e}^{j3\arg\underline{V}_y} \tag{14b}$$
$$\underline{E}_{s,n} = j\frac{\underline{I}\,|\underline{V}_y|}{12\omega}\mathrm{e}^{-j3\arg\underline{V}_y} - j\frac{\underline{V}_y^*\underline{I}^*}{2\omega} \tag{14c}$$
$$\underline{E}_d = -j\frac{v_\mathrm{DC}\underline{I} - 2I_{s0}\underline{V}_{y\Delta}}{\omega}. \tag{14d}$$

While the constants (14) are fixed by $\underline{I}$ and $\underline{V}_y$, the stored energy E_{s0} must be higher than its equilibrium $E_{s0,\mathrm{eq}} = 2Cv_\mathrm{DC}^2$ to guarantee enough voltage on the cells. To sum up, stationary operation with triplen harmonic injection and zero circulating current is linked to the set of constants (14). This beneficial property of (13) is used in Section III-A to derive nonstationary solutions of (6).

D. Parameterization Via e_{s0}, $\underline{e}_s$, and e_{d0}

The power balance (6a) can be used to obtain the (scaled) dc current

$$i_{s0} = \frac{\dot{e}_{s0} + \mathrm{Re}\big(\underline{i}\,\underline{v}_y^*\big)}{v_\mathrm{DC}} \tag{15}$$

while its driving voltage v_{x0} can be calculated from (8b) once the derivative of (15) has been inserted. Excluding the singularity $i_{s0} = 0$, the subsystem (6b) yields the common-mode voltage

$$v_{y0} = -\frac{\dot{e}_{d0} + \mathrm{Re}\big(\underline{i}_s^*\underline{v}_{y\Delta}\big)}{2i_{s0}} \tag{16}$$

which can be used to eliminate v_{y0} from the subsystem (6c) describing $\underline{e}_s$. The resulting equation can be solved for the circulating current

$$\underline{i}_s = \frac{j\mathrm{Im}(\underline{i}\,\underline{C}^*(\underline{e}_s,\dot{\underline{e}}_s))\,\underline{v}_{y\Delta} - v_\mathrm{DC}(i_{s0}\,\underline{C}(\underline{e}_s,\dot{\underline{e}}_s) + \dot{e}_{d0}\underline{i})}{v_\mathrm{DC}\mathrm{Re}\Big(\underline{i}\,\underline{v}_{y\Delta}^*\Big) + i_{s0}v_\mathrm{DC}^2} \tag{17}$$

with

$$\underline{C}(\underline{e}_s,\dot{\underline{e}}_s) = -\mathrm{e}^{-j3\theta}\underline{v}_y^*\underline{i}^* - \dot{\underline{e}}_s - j\omega\underline{e}_s \tag{18}$$

which completes the solution of v_{y0} once (17) has been inserted back into (16). The driving voltage $\underline{v}_x$ of the circulating current is obtained from its dynamics (8a) and the time derivative of (17). This implies that the MMC variables i_{s0}, $\underline{i}_s$, v_{y0}, and v_{x0} are specified via trajectories for the energies e_{s0}, $\underline{e}_s$, and e_{d0} and the time-dependent parameter $\underline{i}$. The evolution of the complex

energy difference $\underline{e}_d$ is fixed as well, because all information is at hand to solve subsystem (6d) by rewriting it in the form

$$\dot{\underline{e}}_d = \dot{\underline{a}}\mathrm{e}^{-j\theta} - j\omega\underline{e}_d. \tag{19}$$

The abbreviation $\dot{\underline{a}}$ reads

$$\dot{\underline{a}} = \left[v_{\mathrm{DC}}\underline{i} - \mathrm{e}^{-j3\theta}\underline{i}_s^*\underline{v}_{y\Delta}^* - 2\underline{i}_s v_{y0} - 2i_{s0}\underline{v}_{y\Delta}\right]\mathrm{e}^{j\theta} \tag{20}$$

and is given by the abovementioned parameterization. Now, $\underline{a}$ is obtained via integration of (20), yielding the solution

$$\underline{e}_d = \underline{a}\mathrm{e}^{-j\theta}. \tag{21}$$

The constant of integration is fixed by the initial value of the complex energy difference $\underline{e}_d$.

III. Optimization

A. Transitions Between Stationary Operating Regimes

One goal of the energy balancing is to restore a balanced operation after a load step. Once a transition of the load has been planned, e.g., as described in Section II-B, a corresponding transfer for the energies needs to be found. Thanks to the parameterization from Section II-D, the energies e_{s0}, $\underline{e}_s$, and e_{d0} (i.e., all energies except for the complex difference $\underline{e}_d$) can still be specified. In order to perform the transfer, the function

$$\mathrm{fade}(\underline{A}, \underline{B}) = \underline{A}F_2(1-\tau_{\mathrm{MMC}}) + \underline{B}F_2(\tau_{\mathrm{MMC}}) \tag{22}$$

is introduced, using the normalized time $\tau_{\mathrm{MMC}} = t/T_{\mathrm{MMC}}$ to fade during $0 < \tau_{\mathrm{MMC}} < 1$ from constant $\underline{A}$ to constant $\underline{B}$ with the raised cosine F_2, defined in Table I and depicted in Fig. 3(b) and its flipped form, respectively. The cross-fading starts together with the load transfer (10) and is allowed to end at the same time or later, which is reflected by the choice $T_{\mathrm{MMC}} \geq T_L$. The candidate transfer employs this function to fade between two stationary solutions (13a)–(13c) defined by the corresponding constants (14) and augments it with additional terms as

$$\begin{aligned} e_{s0,\mathrm{d}} &= \mathrm{fade}(A_{s0}, B_{s0}) \\ &\quad + C_{s0}F_3(\tau_{\mathrm{L}}) + D_{s0}F_3(1-\tau_{\mathrm{L}}) \end{aligned} \tag{23a}$$

$$e_{d0,\mathrm{d}} = \mathrm{Re}\left\{\mathrm{fade}(\underline{A}_{d0}, \underline{B}_{d0})\mathrm{e}^{j3\theta} - H\frac{\underline{e}_K\underline{v}_g^*}{v_{\mathrm{DC}}}\right\} \tag{23b}$$

$$\begin{aligned} \underline{e}_{s,\mathrm{d}} &= \mathrm{fade}(\underline{A}_{s,p}, \underline{B}_{s,p})\mathrm{e}^{j3\theta} + \mathrm{fade}(\underline{A}_{s,n}, \underline{B}_{s,n})\mathrm{e}^{-j3\theta} \\ &\quad + \underline{C}_s F_3(\tau_{\mathrm{L}}) + \underline{D}_s F_3(1-\tau_{\mathrm{L}}) + \underline{e}_K \end{aligned} \tag{23c}$$

with $H \in \{0, 1\}$, and

$$\underline{e}_K = \underline{K}\left[F_2(2\tau_{\mathrm{MMC}}) + F_2(1-2\tau_{\mathrm{MMC}}) - 1\right]\mathrm{e}^{-j2\theta}. \tag{24}$$

The constants A_{s0}, $\underline{A}_{d0}$, $\underline{A}_{s,p}$ and $\underline{A}_{s,n}$ correspond to the constants E_{s0}, and (14) of the stationary operation (13) before the transfer, i.e., for $\tau_{\mathrm{MMC}} < 0$, and B_{s0}, $\underline{B}_{d0}$, $\underline{B}_{s,p}$, and $\underline{B}_{s,n}$ constitute the operation after the transfer, i.e., for $\tau_{\mathrm{MMC}} > 1$. Having the basic idea of [26] in mind, the total stored energy is adapted via A_{s0} and B_{s0} to the output voltage amplitude and load in order to take advantage of the full interval of the duty cycle. The constants C_{s0}, $\underline{C}_s$, D_{s0}, and $\underline{D}_s$ are of lower importance for understanding the basic idea but are included for completeness. They are used to maintain smoothness of the dc current (15) and circulating current (17) with the help of F_3 (see Table I and Fig. 3(c)) in case of discontinuities in the nominal load voltage $\underline{v}_y$ caused by the linear transfer (10) for the load. By choosing $H = 0$, the candidate transfer (23) is similar to the one from [24], whereas $H = 1$ offers an improved behavior of the common-mode voltage. The constant $\underline{K} \in \mathbb{C}$ is dedicated to indirectly steer the vertical difference $\underline{e}_d$ that cannot be specified freely because all degrees of freedom are already used up by (23). The use of $\underline{K}$ and the benefits of $H = 1$ are demonstrated in the next section.

This leaves F_2, F_3, and the complex exponentials as the only time-dependent part of the candidate transfer (23), whose time derivatives can now be easily obtained because all other parameters are constant during each transfer. This paves the way for the parameterizations (15)–(17), to obtain nominal trajectories for the currents (8) and their driving voltages. With these results, the corresponding nominal trajectory for the complex difference $\underline{e}_d$ can be obtained by (21), where $\underline{a}$ can be calculated via integration of $\dot{\underline{a}}$ defined in (20) after all variables have been substituted by their nominal ones. As a result, the nominal trajectory of $\underline{e}_d$ can be expressed as

$$\underline{e}_{d,\mathrm{d}} = \underline{a}(\underline{K})\mathrm{e}^{-j\theta}. \tag{25}$$

Explicit dependence of $\underline{a}$ from the trajectory parameter $\underline{K}$ indicates its dedicated purpose to influence the nominal trajectory $\underline{e}_{d,\mathrm{d}}$, which is demonstrated next.

B. Optimized Feedforward Balancing

The purpose of the constant $\underline{K}$ is to steer the otherwise uncontrolled energy $\underline{e}_d$ into the stationary operation $\underline{E}_d$ at the end of the transfer. This is depicted in Fig. 4 where the same transition of the load is shown for three cases.

1) Fig. 4(a) serves as a reference, because balancing is disabled by setting $\underline{K} = 0$. Although the load current and the energies $\underline{e}_{s,\mathrm{d}}$ and $e_{d0,\mathrm{d}}$ reach the desired operation, the complex energy difference $\underline{e}_{d,\mathrm{d}}$ misses the stationary solution $\underline{E}_d$ at $t = T_{\mathrm{MMC}}$ shown in gray. This results in an indefinite unbalanced operation, as one can see from the equivalent cell voltages at the bottom.
2) Fig. 4(b) depicts the same transfer but this time an optimized choice of $\underline{K}$ introduces a detour in the complex sum $\underline{e}_{s,\mathrm{d}}$ indirectly steering $\underline{e}_{d,\mathrm{d}}$ into stationary operation for $t \geq T_{\mathrm{MMC}}$. The corresponding equivalent cell voltages at the bottom confirm balanced operation. This comes at the price of an elevated amplitude of the common-mode voltage v_{y0} as one can see in the second to last row in Fig. 4(b) and originates from the trajectory for the vertical difference energy e_{d0} depicted in the third row of Fig. 4(b) that was obtained by just fading from one stationary solution to the other. This common-mode voltage v_{y0} requires a higher reserve in the modulation index and has limited practical merit for grid-side applications.
3) In order to avoid this, an alternative trajectory for the vertical difference e_{d0}, enabled by $H = 1$, has proven good results, as can be seen in Fig. 4(c). The idea of the additional part in (23b) is to allow a larger temporary deviation compared to the case $H = 0$ in favor of a lower

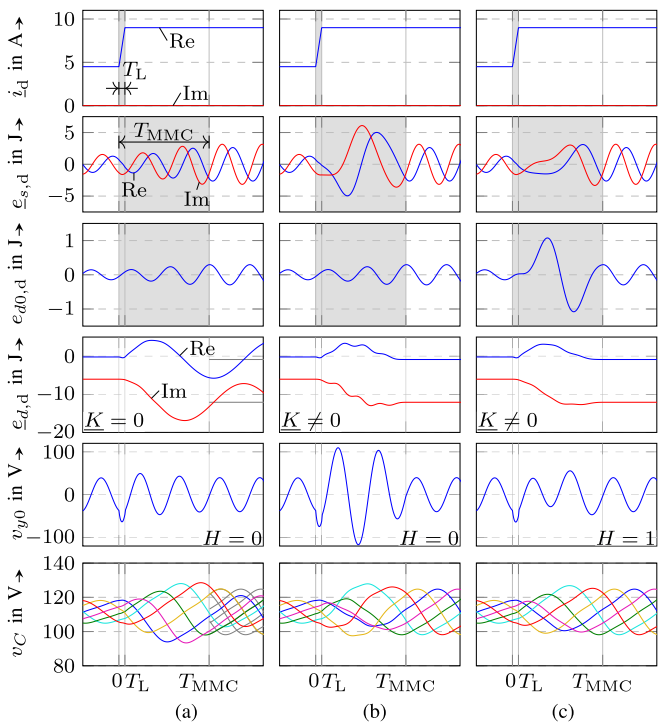

Fig. 4. Three different energy transfers (second and third row) for the same load step (first row): (a) without balancing, (b) with balancing, and (c) with improved common-mode voltage. In all cases, the stored energy is $e_{s0} = 56$ J.

common-mode voltage. This is an improvement over the trajectory candidate from [24].

In either choice of the option $H \in \{0, 1\}$, the value of $\underline{K}$ must be adapted to the respective reference trajectory of the load (10) and the desired duration T_{MMC} of the energy transition (23). Here, $\underline{K}$ is found by minimizing the cost function

$$G(\underline{K}) = \left|\underline{E}_d - \underline{e}_{d,\mathrm{d}}(\underline{K}, T_{\mathrm{MMC}})\right| \tag{26}$$

in which the complex energy difference at the end of the (candidate) transfer $\underline{e}_{d,\mathrm{d}}(\underline{K}, T_{\mathrm{MMC}})$ is given by (25). Owing to the strategy presented here, obtaining a nonstationary nominal solution of (6) and (8) boils down to algebraic expressions in the nominal trajectories and their easily obtained derivatives and just one open-loop integration of a complex variable. This is the lowest known order of the internal dynamics for an ac current controlled MMC [27] and significantly speeds up the optimization.

The selected trajectories enable a seamless transfer between the two stationary solutions, while at the same time, the MMC energies are balanced via feedforward circulating current and common-mode voltage.

In conclusion, the proposed planning-based feedforward balancing scheme enables fast transitions into new operating regimes after load changes by means of consistent references for the MMC variables. Fast transitions are required during low-voltage fault ride-through (FRT) as well, and in general, a similar improvement is to be expected there. However, the present implementation is unable to operate at zero active power, as may be the case during an FRT event, because it relies on the parameterization (16), which suffers from a singularity when the dc current is zero, i.e., when $i_{s0} = 0$. This is a limitation of the particular parameterization but not a limitation of the general methodology because an alternative parameterization could be used to avoid the singularity. In contrast to a load change command, a short delay is to be expected in case of an FRT event, because the trajectory planning would start after detecting the low-voltage condition. However, during replanning, the feedback control already reacts to the disturbance as shown in [28] for a different setup.

C. Feedback Balancing

Only nominal behavior was considered when planning the transitions, and thus a balancing feedback will be used to deal with small deviations from the reference trajectories. The balancing feedback

$$\underline{i}_{s,b} = \underset{\text{horizontal}}{k_s\, \underline{e}_{s,\mathrm{err}}} - \underset{\text{vertical (neg. seq.)}}{k_d \underline{e}^*_{d,\mathrm{err}} \mathrm{e}^{-j(3\theta+\varphi_d)}} - \underset{\text{vertical (pos. seq.)}}{k_0 e_{d0,\mathrm{err}} \mathrm{e}^{j\varphi_0}} \tag{27}$$

acts on the circulating current $\underline{i}_s$ via dedicated energy errors amplified by the proportional gains k_s, k_d, and k_0. The phase-shifting angles φ_d and φ_0 are used to maximize the respective balancing effect with respect to the alignment of the output voltage $\underline{v}_y$ and in the presence of the mutual inductance M_z. Usually, the errors $\underline{e}_{d,\mathrm{err}} = \underline{e}_{d,\mathrm{ref}} - \underline{e}_d$, $\underline{e}_{s,\mathrm{err}} = \underline{e}_{s,\mathrm{ref}} - \underline{e}_s$, and $e_{d0,\mathrm{err}} = e_{d0,\mathrm{ref}} - e_{d0}$ are obtained with respect to a stationary operating regime, i.e., the references $\underline{e}_{s,\mathrm{ref}}$, $\underline{e}_{d,\mathrm{ref}}$, and $e_{d0,\mathrm{ref}}$ are given by a stationary operating regime like (13). Except for the use of a different reference frame, the balancing feedback (27) with a stationary operating regime as reference equals the *hf-mode* in [16] and provides very good balancing. This setting is called *standard balancing*.

When the optimized trajectories are used, the balancing references are set to $\underline{e}_{s,\mathrm{ref}} = \underline{e}_{s,\mathrm{d}}$ and $e_{d0,\mathrm{ref}} = e_{d0,\mathrm{d}}$, whereas $\underline{e}_{d,\mathrm{ref}}$ is obtained from (21). This setting provides an optimized feedforward balancing and would ideally result in zero balancing feedback (27).

IV. Experimental Results

The goal of the measurements is to compare the standard balancing with the augmented balancing scheme in order to investigate the effect of optimized feedforward circulating currents and common-mode voltages and to evaluate the expected planning improvements for grid-side applications. The block diagram in Fig. 5 depicts the implemented balancing scheme. In order to simplify the diagram, the current controllers have been incorporated into the block of the MMC model. The block diagram in Fig. 6 depicts the implementation of the energy references and the corresponding optimized common-mode voltage and circulating current. The variable $F \in \{0, 1\}$ is used to switch between the following two cases.

1) *Standard balancing ($F = 0$):* The balancing relies on the feedback (27) only. In this configuration, the balancing controller is responsible for stationary operation and large signal transfer induced by sudden changes in the operating regime.

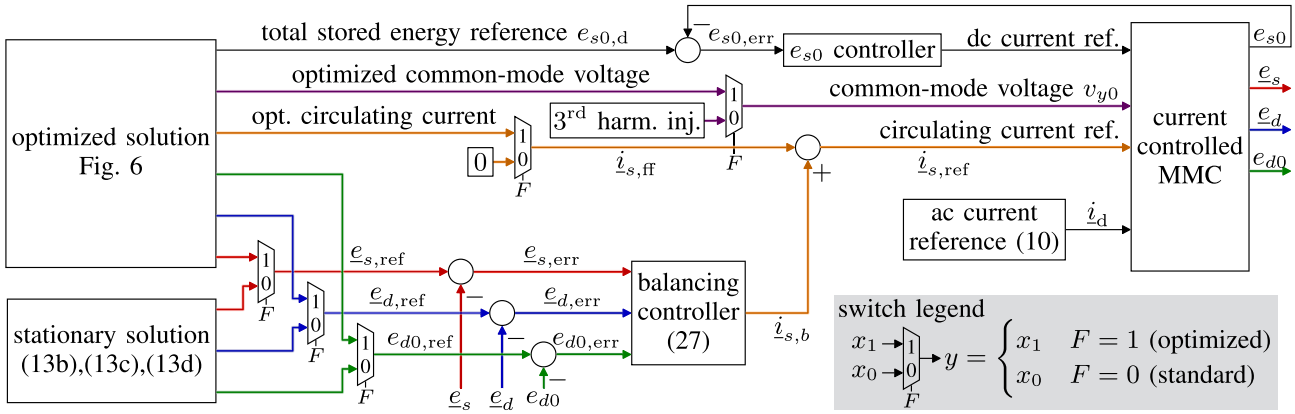

Fig. 5. Block diagram of the standard (i.e., $F = 0$) and optimized (i.e., $F = 1$) energy balancing scheme [24].

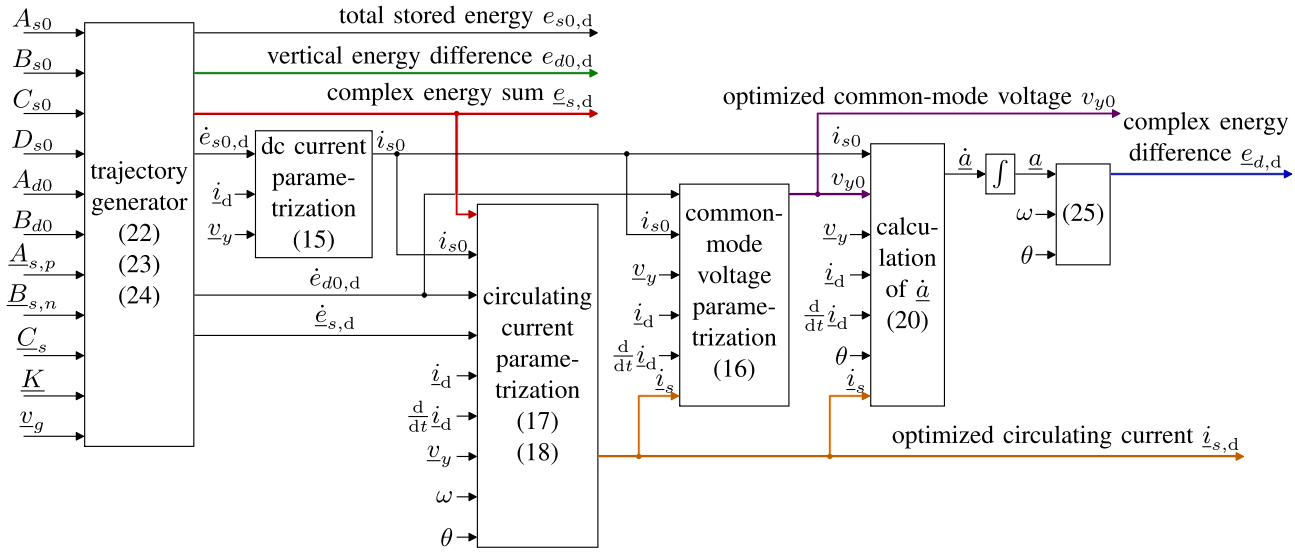

Fig. 6. Block diagram for the implementation of the optimized solution: the trajectory generator provides the references and their analytically obtained derivatives that are needed to calculate the corresponding nominal variables and the complex energy difference.

2) *Optimized balancing ($F = 1$):* An optimized solution is used to reach the new stationary operation in finite time by injecting the corresponding feedforward circulating current and common-mode voltage. The balancing feedback (27) permanently rejects small control errors with respect to the optimized solution. In case of ideal open-loop control, the balancing feedback is zero, i.e., $\underline{i}_{s,b} = 0$, even during the transfer between operating regimes.

The balancing scheme was tested on a low-voltage test bench in two setups: first, feeding an RL load, as described in Section IV-A; and second, as a grid-side converter feeding a dc load, as described in Section IV-B.

A. *RL Load*

During the preparation of this paper, we identified an error in the implementation used for $F = 0$ in [24] causing a wrong value for the stationary reference $e_{d0,\mathrm{ref}}$. The measurements for $F = 1$ were not affected. Figs. 7–9 show the experimental results for the corrected version on the left and a rerun of the optimized balancing on the right, in which the MMC described in Table II feeds an RL load as given in Table III at $\omega = 2\pi$ 50.875 Hz. The proportional gains of the balancing

TABLE II
PARAMETERS OF THE MMC FOR THE EXPERIMENTS

	Symbol	Value
Number of cells per arm	n	6
Cell capacitance	nC	375 μF
Arm inductor	L_z	1.2 mH
Mutual inductance	M_z	0.94 mH
Controller update rate		4.884 kHz

TABLE III
PARAMETERS FOR THE MEASUREMENTS

	$k_0/(\mathrm{V{\cdot}s})$	$k_s/(\mathrm{V{\cdot}s})$	$k_d/(\mathrm{V{\cdot}s})$	R/Ω	L/mH	$\lvert\underline{v}_g\rvert/\mathrm{V}$
Figs. 7–9	2	5	4	26.6	3.14	0
Figs. 10–12	0.61	0.18	0.55	0	15	235

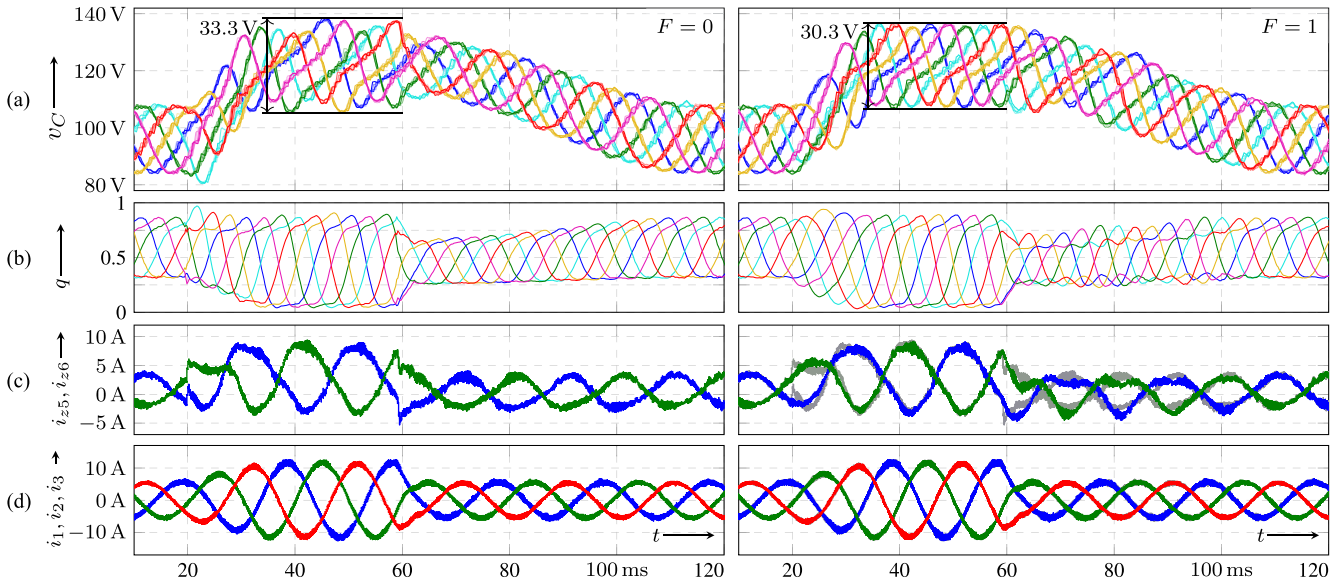

Fig. 7. Measurement results for RL load without (left) and with feedforward (right): (a) cell voltages, (b) normalized arm voltage commands, (c) two arm currents, and (d) output currents. The left current measurements are shown again in gray on the right to facilitate comparison.

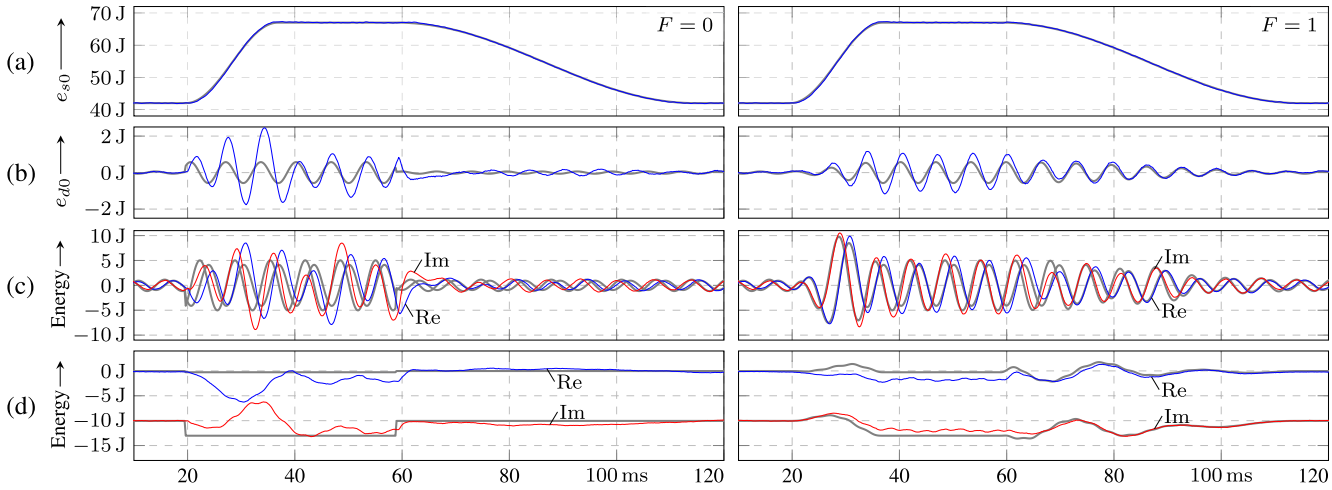

Fig. 8. Measurement results of the energies for an RL load without (left) and with feedforward (right): (a) total stored energy e_{s0}, (b) vertical difference e_{d0}, (c) complex sum $\underline{e}_s$, and (d) complex difference $\underline{e}_d$. The nominal values are shown in gray.

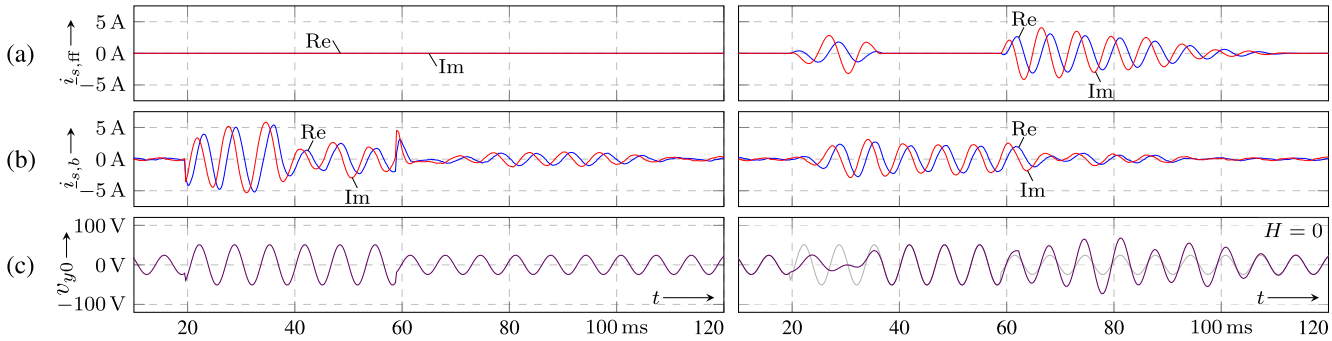

Fig. 9. Measurement of circulating current and common-mode voltage without (left) and with feedforward (right): (a) feedforward circulating current, (b) balancing feedback, and (c) common-mode voltage. Thanks to the feedforward circulating current, the balancing feedback is reduced to the level required for the rejection of disturbances. In addition to that, the optimized common-mode voltage contributes to the balancing. The bottommost trace on the left is shown again in gray on the right.

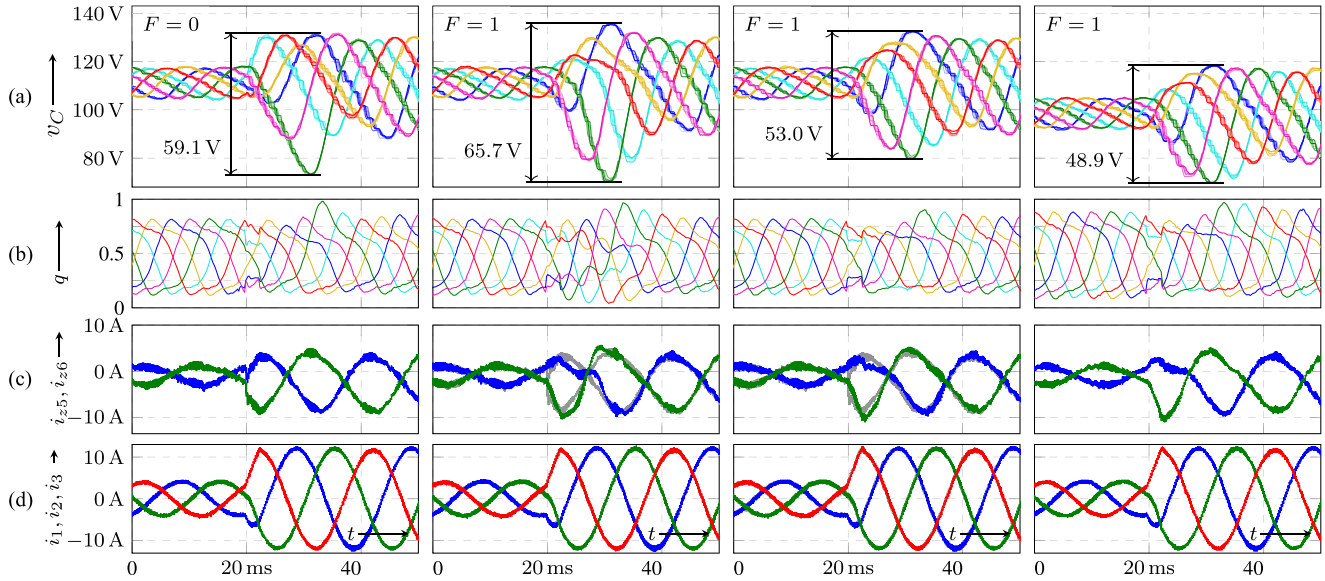

Fig. 10. Measurement results without (left) and with feedforward (three rightmost columns): (a) cell voltages, (b) normalized arm voltage commands, (c) two arm currents, and (d) output currents. The left current measurements are shown again in gray in the middle and right side to facilitate comparison.

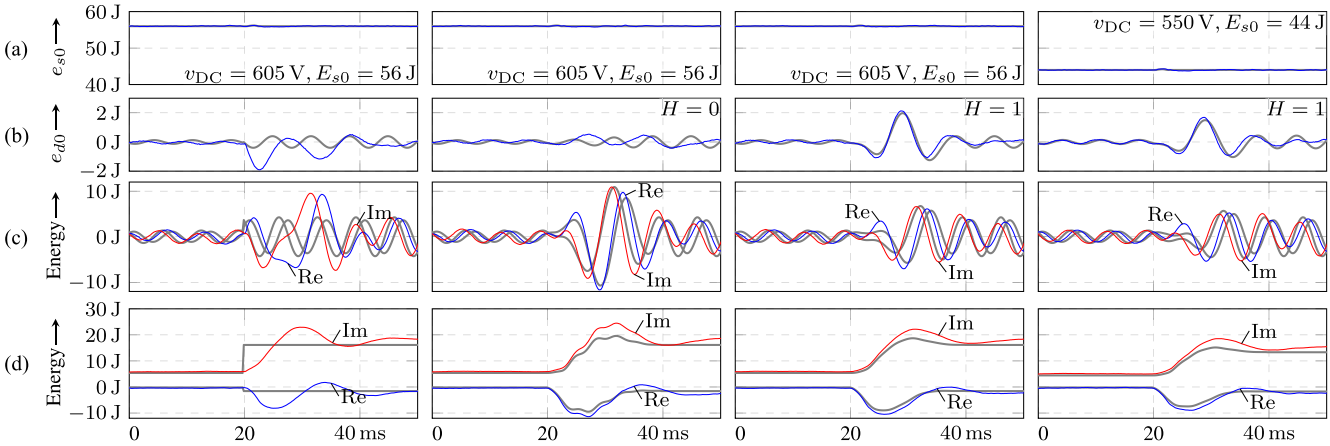

Fig. 11. Measurement results of the energies without (left) and with feedforward (three rightmost columns): (a) total stored energy e_{s0}, (b) vertical difference e_{d0}, (c) complex sum $\underline{e}_s$, and (d) complex difference $\underline{e}_d$. The corresponding reference values for the energies are shown in gray in rows (a)–(d).

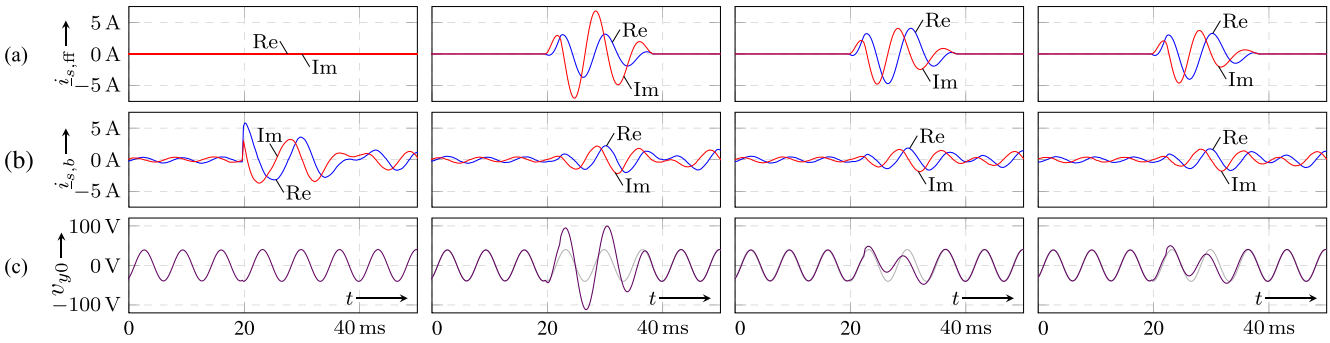

Fig. 12. Measurement of circulating current and common-mode voltage without (left) and with feedforward (right): (a) feedforward circulating current, (b) balancing feedback, and (c) common-mode voltage. The bottommost trace on the left is shown again in gray on the right.

feedback (27) are given in Table III and the current was increased and decreased between 3.9 and 8.1 A. In comparison to the standard balancing on the left column in Fig. 7, the optimized scheme is able to retain balanced capacitor voltages even during the transfers and enters the stationary operation in finite time, whereas the standard balancing needs more time to reach the new operating regime. Thanks to the optimized balancing, a reduction in the cell-voltage spread of almost 10% is achieved, as depicted in Fig. 7(a). The corresponding measurements of the transformed arm energies in Fig. 8 confirm that the optimized

trajectories are tracked closer, owing to the feedforward circulating currents and common-mode voltage, as shown in Fig. 9. Thanks to the feedforward circulating current in Fig. 9(a), the balancing feedback in Fig. 9(b) is reduced to the level required for the rejection of disturbances. In addition to that, the optimized common-mode voltage, shown in Fig. 9(c), contributes to the balancing.

The excessively slow cross-fading of the two stationary operating regimes during 60 ms $< t <$ 110 ms results in an artificial stretch of the nonstationary operation and demonstrates the steering performance of the optimized balancing, at the cost of an increased feedforward circulating current $\underline{i}_{s,\mathrm{ff}}$, visible in the right column of Fig. 9(a). This gives the standard balancing a slight advantage during the slow decrease of the stored energy, because the stationary references coincide earlier to the reduced load at $t \approx 60$ ms.

B. Grid-Side Application

In a second setup, the MMC from Table II was feeding a dc load in a grid-side configuration. In contrast to the previous experiment, the frequency ω and angle θ are given by the grid and measured by means of a phase-locked loop, however, during optimization, the nominal frequency $\omega = 2\pi$ 50 Hz is used. The measurement results of four experiments are shown in Figs. 10–12 where the load was increased from 2.83 to 8.49 A and the gains were set according to Table III to account for the grid voltage $\underline{v}_g$.

Standard balancing ($F = 0$) is used in the first experiment, shown in the leftmost column and provides a basis for comparison. The maximum spread of the capacitor voltages is 59.1 V and the major fraction of the balancing error decays during the grid voltage period after the transition of the load, as visible from the transformed arm energies in the leftmost column of Fig. 11. In Fig. 12(b), the increased balancing effort of the feedback (27) is visible as expected due to the absence of a feedforward circulating current.

The optimized balancing ($F = 1$) with $H = 0$ is shown in the second column of Figs. 10–12 and features symmetric capacitor voltages during the transition, at the cost of an undesirable increase in their spread to 65.7 V. Apart from a reduced deviation of the vertical difference e_{d0} and a slightly better reserve at the upper limits of the duty cycles in Fig. 10(b), this offers no benefits over the standard balancing. This can be attributed to the suboptimal behavior of the common-mode voltage for grid-side applications, which is caused by the overly balanced vertical energy e_{d0} and was mentioned in Section III-B.

The optimized balancing ($F = 1$) with $H = 1$ for improved common-mode voltage is not only able to overcome this problem but even reduces the capacitor voltage spread during the transfer, as shown in the third columns of Figs. 10–12. The intended deviation of the vertical difference e_{d0}, visible in the third column of Fig. 10(c), leaves the common-mode voltage v_{y0} close to the waveform required for triplen harmonic injection, and at the same time, reduces the feedforward circulating current compared to the previous approach, as shown in Fig. 12(c) and (a), respectively. Even the feedback component of the circulating current is slightly reduced in comparison to the second configuration. The traces of the duty cycles in Fig. 10(b) reveal an increased reserve at their upper and lower limits, allowing for a reduction in both, the stored energy e_{s0} and the dc voltage v_{DC}, which is shown in the rightmost column of Figs. 10–12. A further reduction in the capacitor voltage spread down to 48.9 V was achieved, even though the load was adapted to the reduced dc voltage in order to give the same ac currents. The duty cycles of the standard balancing in the left column of Fig. 10(b) are already close to the upper limit and would saturate with the reduced energy and dc voltage.

V. Conclusion

An optimized MMC energy balancing scheme was proposed that utilizes feedforward circulating currents and common-mode voltage. The ac current controlled MMC was chosen as an example, due to the challenging nature of the feedforward calculation that lies in the problem of controlling six energies with as few as four independent inputs, namely three currents and the common-mode voltage. Thanks to the planning approach of specifying candidate trajectories for a maximized subset of transformed arm energies, only one complex energy variable needs to be obtained via integration which speeds up the optimization due to the significant calculation cost reduction.

A new set of candidate trajectories was proposed that brings the common-mode voltage waveform during transfers close to the desired triplen harmonic injection, which is especially useful in grid-side applications where just a small reserve in the modulation index is available. A reduction in the cell-voltage spread for the optimized schemes was demonstrated in comparison to the standard balancing for an RL load and a grid-side setup. Due to the improved common-mode voltage in the grid-side experiment, a reduction in the stored energy and in the dc voltage was achieved even with the same power. The experiments demonstrate a reduced current contribution of the balancing feedback when the optimized references and the feedforward is used.

Future research will focus on extending the operating region and on resolving the active power constraints of the MMC parameterization.

References

[1] A. Lesnicar and R. Marquardt, "An innovative modular multilevel converter topology suitable for a wide power range," in *Proc. IEEE Bologna Power Tech Conf. Proc.*, vol. 3, 2003.

[2] M. Hiller, D. Krug, R. Sommer, and S. Rohner, "A new highly modular medium voltage converter topology for industrial drive applications," in *Proc. 13th Eur. Conf. Power Electron. Appl.*, Sep. 2009.

[3] S. Rohner, J. Weber, and S. Bernet, "Continuous model of modular multilevel converter with experimental verification," in *Proc. IEEE Energy Convers. Congr. Expo.*, Sep. 2011, pp. 4021–4028.

[4] R. Marquardt, "Modular multilevel converter: An universal concept for HVDC-networks and extended DC-bus-applications," in *Proc. Int. Power Electron. Conf.* Sapporo, Japan, Jun. 2010, pp. 502–507.

[5] M. A. Pérez, S. Bernet, J. Rodríguez, S. Kouro, and R. Lizana, "Circuit topologies, modeling, control schemes, and applications of modular multilevel converters," *IEEE Trans. Power Electron.*, vol. 30, no. 1, pp. 4–17, Jan. 2015.

[6] M. Lu, J. Hu, R. Zeng, and Z. He, "Fundamental-frequency reactive circulating current injection for capacitor voltage balancing in hybrid-MMC HVDC systems during riding through PTG faults," *IEEE Trans. Power Del.*, Sep. 2017, doi: 10.1109/TPWRD.2017.2755505.

[7] S. Cui and S.-K. Sul, "A comprehensive DC short-circuit fault ride through strategy of hybrid modular multilevel converters (MMCs) for overhead line transmission," *IEEE Trans. Power Electron.*, vol. 31, no. 11, pp. 7780–7796, Nov. 2016.
[8] T. Soong and P. W. Lehn, "Internal power flow of a modular multilevel converter with distributed energy resources," *IEEE J. Emerg. Sel. Topics Power Electron.*, vol. 2, no. 4, pp. 1127–1138, Dec. 2014.
[9] G. Henke and M.-M. Bakran, "Balancing of modular multilevel converters with unbalanced integration of energy storage devices," in *Proc. 18th Eur. Conf. Power Electron. Appl.*, Karlsruhe, Germany, Sep. 2016.
[10] M. Jankovic, A. Costabeber, A. Watson, and J. C. Clare, "Arm-balancing control and experimental validation of a grid-connected MMC with pulsed DC load," *IEEE Trans. Ind. Electron.*, vol. 64, no. 12, pp. 9180–9190, Dec. 2017.
[11] L. Ängquist, A. Antonopoulos, D. Siemaszko, K. Ilves, M. Vasiladiotis, and H.-P. Nee, "Inner control of modular multilevel converters—An approach using open-loop estimation of stored energy," in *Proc. 2010 Int. Power Electron. Conf.*, Sapporo, Japan, Jun. 2010, pp. 1579–1585.
[12] A. J. Korn, M. Winkelnkemper, and P. Steimer, "Low output frequency operation of the modular multi-level converter," in *Proc. IEEE Energy Convers. Congr. Expo.*, Atlanta, GA, USA, Sep. 2010, pp. 3993–3997.
[13] P. Münch, D. Görges, M. Izák, and S. Liu, "Integrated current control, energy control and energy balancing of modular multilevel converters," in *Proc. 36th Annu. Conf. IEEE Ind. Electron. Soc.*, Glendale, AZ, USA, 2010, pp. 150–155.
[14] S. P. Engel and R. W. De Doncker, "Control of the modular multi-level converter for minimized cell capacitance," in *Proc. 14th Eur. Conf. Power Electron. Appl.*, Birmingham, U.K., Aug. 2011.
[15] G. Bergna *et al.*, "A generalized power control approach in ABC frame for modular multilevel converter HVDC links based on mathematical optimization," *IEEE Trans. Power Del.*, vol. 29, no. 1, pp. 386–394, Feb. 2014.
[16] J. Kolb, F. Kammerer, M. Gommeringer, and M. Braun, "Cascaded control system of the modular multilevel converter for feeding variable-speed drives," *IEEE Trans. Power Electron.*, vol. 30, no. 1, pp. 349–357, Jan. 2015.
[17] H. R. Parikh, R. S. M. Loeches, G. Tsolaridis, R. Teodorescu, L. Mathe, and S. Chaudhary, "Capacitor voltage ripple reduction and arm energy balancing in MMC-HVDC," in *Proc. IEEE 16th Int. Conf. Environ. Elect. Eng.*, Florence, Italy, Jun. 2016.
[18] Y. Okazaki, H. Matsui, M. M. Muhoro, M. Hagiwara, and H. Akagi, "Capacitor-voltage balancing for a modular multilevel DSCC inverter driving a medium-voltage synchronous motor," *IEEE Trans. Ind. Appl.*, vol. 52, no. 5, pp. 4074–4083, Sep. 2016.
[19] F. Deng and Z. Chen, "Voltage-balancing method for modular multilevel converters under phase-shifted carrier-based pulsewidth modulation," *IEEE Trans. Ind. Electron.*, vol. 62, no. 7, pp. 4158–4169, Jul. 2015.
[20] N. Stanković, G. Bergna, A. Arzandé, E. Berne, P. Egrot, and J.-C. Vannier, "An optimization-based control strategy for modular multilevel converters: design and implementation," in *Proc. IEEE 11th Int. Conf. Power Electron. Drive Syst.*, Sydney, NSW, Australia, Jun. 2015, pp. 12–17.
[21] J. Pou, S. Ceballos, G. Konstantinou, V. G. Agelidis, R. Picas, and J. Zaragoza, "Circulating current injection methods based on instantaneous information for the modular multilevel converter," *IEEE Trans. Ind. Electron.*, vol. 62, no. 2, pp. 777–788, Feb. 2015.
[22] C. Zhao, Y. Li, F. Xu, Z. Li, P. Wang, and M. Lei, "Capacitor voltage ripples characterization and reduction of hybrid modular multilevel converter with circulating current injection," in *Proc. IEEE Energy Convers. Congr. Expo.*, Cincinnatti, OH, USA, Oct. 2017, pp. 4560–4567.
[23] H. Fehr, A. Gensior, and M. Müller, "Analysis and trajectory tracking control of a modular multilevel converter," *IEEE Trans. Power Electron.*, vol. 30, no. 1, pp. 398–407, Jan. 2015.
[24] H. Fehr and A. Gensior, "Improved energy balancing for modular multilevel converters by optimized feed-forward circulating currents and common mode voltage," in *Proc. 19th Eur. Conf. Power Electron. Appl.*, Warsaw, Poland, Sep. 2017.
[25] H. Bärnklau, A. Gensior, and S. Bernet, "Derivation of an equivalent submodule per arm for modular multilevel converters," in *Proc. 15th Int. Power Electron. Motion Control Conf.*, Novi Sad, Serbia, 2012, pp. LS2a.2-1–LS2a.2-5.
[26] A. Antonopoulos, L. Ängquist, L. Harnefors, and H.-P. Nee, "Optimal selection of the average capacitor voltage for variable-speed drives with modular multilevel converters," *IEEE Trans. Power Electron.*, vol. 30, no. 1, pp. 227–234, Jan. 2015.
[27] H. Bärnklau, A. Gensior, and J. Rudolph, "A model-based control scheme for modular multilevel converters," *IEEE Trans. Ind. Electron.*, vol. 60, no. 12, pp. 5359–5375, Dec. 2013.
[28] H. Fehr and A. Gensior, "On trajectory planning, backstepping controller design and sliding modes in active front-ends," *IEEE Trans. Power Electron.*, vol. 31, no. 8, pp. 6044–6056, Aug. 2016.

Hendrik Fehr received the Dipl.-Ing. degree in Elektrotechnik from the Technische Universität Dresden (TU Dresden), Dresden, Germany, in 2008.

He is currently with the Professur Leistungselektronik, Elektrotechnisches Institut, TU Dresden. His research interests include modulation and control of power electronic converters, sliding mode, and flatness-based methods.

Albrecht Gensior received the Dipl.-Ing. and Dr.-Ing. degrees in Elektrotechnik from the Technische Universität Dresden (TU Dresden), Dresden, Germany, in 2003 and 2008, respectively.

He is currently with the Professur Leistungselektronik, Elektrotechnisches Institut, TU Dresden, where he is involved in research projects dealing with the control of power electronic converters and drives. His research interests include nonlinear controller design and observers for these applications.